research papers

Transient thermal stress wave and vibrational analyses of a thin diamond crystal for X-ray free-electron lasers under high-repetition-rate operation

Bo Yang,[a]* Songwei Wang[a] and Juhao Wu[b]*

[a]Department of Mechanical and Aerospace Engineering, The University of Texas at Arlington, 500 West First Street, Arlington, TX 76019, USA, and [b]SLAC National Accelerator Laboratory, 2575 Sand Hill Road, Menlo Park, CA 94025, USA. *Correspondence e-mail: boyang@uta.edu, jhwu@slac.stanford.edu

High-brightness X-ray free-electron lasers (FELs) are perceived as fourth-generation light sources providing unprecedented capabilities for frontier scientific researches in many fields. Thin crystals are important to generate coherent seeds in the self-seeding configuration, provide precise spectral measurements, and split X-ray FEL pulses, *etc*. In all of these applications a high-intensity X-ray FEL pulse impinges on the thin crystal and deposits a certain amount of heat load, potentially impairing the performance. In the present paper, transient thermal stress wave and vibrational analyses as well as transient thermal analysis are carried out to address the thermomechanical issues for thin diamond crystals, especially under high-repetition-rate operation of an X-ray FEL. The material properties at elevated temperatures are considered. It is shown that, for a typical FEL pulse depositing tens of microjoules energy over a spot of tens of micrometers in radius, the stress wave emission is completed on the tens of nanoseconds scale. The amount of kinetic energy converted from a FEL pulse can reach up to $\sim$10 nJ depending on the layer thickness. Natural frequencies of a diamond plate are also computed. The potential vibrational amplitude is estimated as a function of frequency. Due to the decreasing heat conductivity with increasing temperature, a runaway temperature rise is predicted for high repetition rates where the temperature rises abruptly after ratcheting up to a point of trivial heat damping rate relative to heat deposition rate.

1. Introduction

Free-electron lasers (FELs) can generate ultra-fast (tens of to a few femtoseconds) coherent high-peak-power (tens to hundreds of gigawatts) radiation pulses over a broad spectral range (infrared to X-ray). The combination of high peak brightness, angstrom wavelengths and femtosecond or sub-femtosecond pulse durations provides the necessary ingredients for pursuing atomic resolution imaging and ultrafast science. Such X-ray FELs have been operating worldwide (Emma *et al.*, 2010; Ishikawa *et al.*, 2012), impacting cutting-edge scientific research. To characterize a high-peak-brightness X-ray FEL, the radiation pulse bandwidth is an important metric. Thus, a high-resolution single-shot spectrometer is needed for its precise measurement. Thin crystals are widely used for this purpose (Yabashi *et al.*, 2006; Zhu *et al.*, 2012; Rehanek *et al.*, 2017). Thin crystals can also serve as monochromators to generate coherent seeds in the self-seeding configuration to improve the X-ray FEL temporal coherence (Geloni *et al.*, 2011; Amann *et al.*, 2012). In other applications,
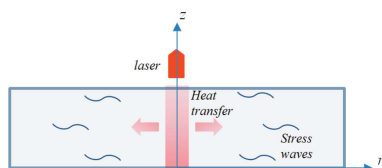
thin crystals are used as X-ray FEL pulse splitters (Zhu *et al.*, 2014). More applications of thin crystals in X-ray FELs are given by Shvyd'ko *et al.* (2017).

When a high-peak-brightness X-ray FEL pulse impinges on such thin crystals, a certain amount of heat is deposited. Adverse effects, including mounting temperature and vibration, may emerge to affect the measurement precision that is sensitive to lattice constant and motion steadiness. Diamond is among the best heat-conducting and mechanically robust solid materials and has been the last reserve for optics use against such adverse effects. Yet there has not been a quantitative or semi-quantitative study to show the magnitudes of the mounting temperature and thermal deformation, not to mention the stress wave dynamics, by considering the realistic material properties of diamond at moderate and elevated temperatures. The thermal expansion dynamics are of general interest and have been studied by using pump–probe high-energy-resolution X-ray diffraction (Stoupin *et al.*, 2012; Navirian *et al.*, 2014). In the present paper, transient thermal stress wave and vibrational analyses as well as transient thermal analysis are carried out to address the potential thermal and mechanical issues in a thin diamond crystal under high-repetition-rate operation of an X-ray FEL. The material properties of diamond, including the thermal expansion and heat capacity (Reeber & Wang, 1996) and thermal conductivity (Wei *et al.*, 1993), valid up to elevated temperatures of 2000–3000 K, are used for the semi-quantitative calculations. The aim is to elucidate the energy transfer mechanisms at the nanosecond level and above in a thin diamond layer and provide insights to the design of thin diamond-based optical devices that can perform under extreme photo-thermo-mechanical loadings.

The rest of the paper is organized as follows. In §2, the problems of transient thermal conduction and stress waves due to instantaneous thermal expansion and steady-state vibration are formulated based on continuum mechanics. The governing equations and relevant material properties of diamond are summarized. In §3, simulation results of a 40 μm-thick plate with a 20 μm waist-size Gaussian beam (relevant to monochromator applications) are presented and discussed, under both single-pulse and multi-pulse inputs. Also, those of a 10 μm-thick plate with 20 μm and 100 μm waist-size and of a 20 μm-thick plate with 20 μm waist-size (relevant to a spectrometer application) are presented and discussed to elucidate the aspect ratio effects on the stress wave dynamics. It is shown that, for a typical FEL pulse releasing tens of microjoules of energy over a spot of tens of micrometers in radius, the stress wave emission is completed at the tens of nanoseconds level. The amount of kinetic energy converted from a FEL pulse can reach up to 10 nJ per pulse. A runaway increase of temperature is observed after a certain number of pulses when the temperature ratchets up to a certain point. It is reached in fewer pulses under a higher repetition rate. This is due to the decreasing thermal conductivity (more precisely, the decreasing thermal diffusivity) with increasing temperature. When the temperature is beyond a critical point, an increase of temperature would lower the diffusivity rather

than enhancing the thermal gradient, resulting in a temperature runaway. Finally, a modal analysis of a millimeter-size plate of various thicknesses is carried out. The possible vibrational amplitude is estimated according to the amount of kinetic energy calculated from the transient simulation. Conclusions are drawn in §4.

2. Problem formulation

2.1. Thermal stress wave emission and conduction

Consider an X-ray FEL pulse passing through a thin crystal and depositing an amount of energy E during its passage, as schematically shown in Fig. 1. The energy from the light is first absorbed by electrons and then transferred to the lattice of the crystal. It is assumed that these processes are undertaken on a timescale of tens of picoseconds. Over that period the lattice is thermalized, but only following this are stress waves of directional motion emitted converting thermal deformation energy into kinetic energy. We aim to analyze the processes of stress wave emission, heat transfer and possible vibrational excitation. A cylindrical coordinate system (r, θ, z) is established with the z-axis normal to the crystal surface. Only a laser beam perpendicular to the crystal surface is considered.

The equation of motion for the crystal is given by

$$\rho \frac{d\mathbf{v}}{dt} = \nabla \cdot \boldsymbol{\sigma}, \tag{1}$$

where ρ is the mass density, $\mathbf{v}$ ($= d\mathbf{u}/dt$) is the velocity, $\mathbf{u}$ is the displacement, $\boldsymbol{\sigma}$ is the stress tensor and t is the time. Assuming isotropic thermoelasticity, the constitutive law is given by (Shorr, 2015)

$$\boldsymbol{\sigma} = 2G\left[\boldsymbol{\varepsilon} - \frac{1}{3}\text{tr}(\boldsymbol{\varepsilon})\mathbf{I}\right] + 3K_{\text{b}}\left[\frac{1}{3}\text{tr}(\boldsymbol{\varepsilon}) - \varepsilon_{\text{T}}\right]\mathbf{I}, \tag{2}$$

where G is the modulus of rigidity, K_{b} is the bulk modulus, $\boldsymbol{\varepsilon}$ $[= (1/2)(\nabla\mathbf{u} + \nabla^{\text{T}}\mathbf{u})]$ is the strain tensor, ε_{T} is the thermal strain, $\mathbf{I}$ is the identity matrix, the superscript T indicates the matrix transpose, and $\text{tr}(\boldsymbol{\varepsilon})$ denotes the trace of $\boldsymbol{\varepsilon}$.

The equation of energy conservation is given by

$$\frac{d(U_{\text{T}} + U_{\varepsilon})}{dt} = -\nabla \cdot (-\kappa \nabla T) + \boldsymbol{\sigma} : \nabla \mathbf{v}, \tag{3}$$
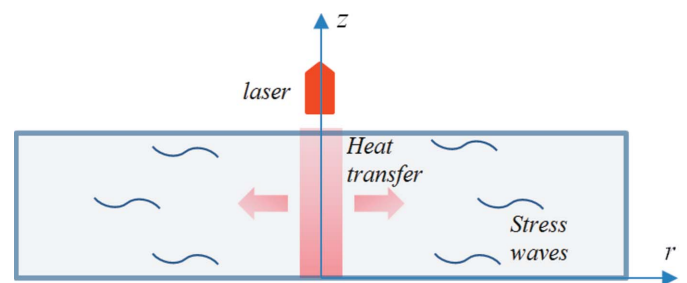

Figure 1
Schematic showing instantaneous heating and subsequent stress wave emission and heat transfer upon laser energy deposition in a thin crystal layer. The cylindrical coordinate system with axisymmetry is established.

where U_T $(= \int \rho C_v \, dT)$ is the thermal energy density, U_ε $[= (1/2)\sigma:(\varepsilon - \varepsilon_T \mathbf{I})]$ is the elastic strain energy density (Mura, 1987), κ is the thermal conductivity and C_v is the specific heat.

The initial displacement and velocity fields are both set equal to zero: $\mathbf{u}_0 = 0$ and $\mathbf{v}_0 = 0$. The initial temperature field is set at $T_0 = 300$ K. Upon a laser pulse, the laser energy is partially absorbed raising the temperature during its passage. The laser beam is assumed to be Gaussian. It impinges perpendicularly to the crystal surface, assumed so that the problem can be reduced to be axisymmetric. The change of thermal energy density as a function of r and z is given by

$$\Delta U_T(r, z) = \frac{2I_0}{\pi a^2 L} \exp\left(-2r^2/a^2\right) \exp(-z/L), \qquad (4)$$

where I_0 is the laser pulse energy, a is the transverse waist-size of the Gaussian beam, and L is the attenuation length. The corresponding temperature increase is determined from the relationship of U_T with T, which is generally a non-linear function.

The traction-free boundary condition, $\boldsymbol{\sigma} \cdot \mathbf{n} = 0$, is applied at all boundaries at all times, where $\mathbf{n}$ is the unit outward normal vector at a surface point. Meanwhile, the boundary condition of zero normal heat flux, $(-\kappa \nabla T) \cdot \mathbf{n} = 0$, is applied at all boundaries at all times.

The above initial-boundary value problem of axisymmetry is numerically solved by applying a finite-volume method (LeVeque, 2002; Versteeg & Malalasekera, 2007). Although the above governing equations are given in the non-conservative form, the corresponding conservative-form equations are coded to solve the problem; there is virtually no difference, since the mass density can be set constant, i.e. the mass conservation equation is not involved, in the case of a solid under low pressure. Briefly, the domain (in the cylindrical reference frame) is discretized in a rectangular mesh of finite volume. The nodes are assigned to the centers of the finite-volume elements. The fluxes of momentum and energy at the boundaries of the finite-volume elements are evaluated by a finite-difference approximation based on nodal values of displacement and energy (temperature). The conservation laws are enforced with these fluxes in a local integral form. By the finite-volume method, the conservation laws are ensured between finite volumes, even though the time derivatives and the fluxes are approximate. For the sake of brevity, the standard procedure of the method is not described in detail herein.

2.2. Modal analysis

Under high-repetition-rate laser pulses, the thin crystal may be excited to vibrate at a non-trivial amplitude, which can be detrimental to any optical component that requires steadiness. The problem may become severe especially when the repetition rate becomes close to any of the resonant frequencies and when the kinetic energy in the system, converted from the laser heat load, cumulates. The plate model is applied to calculate the resonant frequencies of the thin crystal. The governing equations for the in-plane and the flexural modes are given, respectively, by (Donaldson, 2006)

$$\nabla \cdot \bar{\boldsymbol{\sigma}} + \rho \omega^2 \bar{\mathbf{u}} = 0, \qquad (5)$$

$$D \nabla^2 \nabla^2 \bar{\mathbf{w}} = 2\rho h \omega^2 \bar{\mathbf{w}}, \qquad (6)$$

where D is the flexural rigidity, h is the thickness and ω is the angular frequency. Here, all of $\bar{\boldsymbol{\sigma}}$, $\bar{\mathbf{u}}$ and $\bar{\mathbf{w}}$ (the transverse deflection, i.e. the z-component of displacement $\bar{\mathbf{u}}$) should be treated as their amplitude in time harmonics. Only the in-plane components of both displacement $\bar{\mathbf{u}}$ and stress $\bar{\boldsymbol{\sigma}}$ are effective in equation (5), and the out-of-plane component in equation (6). The fully traction-free and the one-edge-clamped boundary conditions will be considered. The above problem is numerically solved by using the commercial finite-element software ANSYS. By decoupling the whole problem in the in-plane and flexural modes as described in equations (5) and (6), those breathing modes corresponding to Lamb's waves with a wavelength comparable with the plate thickness are neglected. For the cases of our interest, those resonant frequencies are in the range of tens of millions of Hertz.

2.3. Materials properties

For diamond, to be analyzed below, the work of Reeber & Wang (1996) is adopted to describe the thermal strain and specific heat capacity. The thermal strain as a function of temperature T is given by

$$\varepsilon_T = \sum_{i=1}^{3} \frac{X_i \theta_i}{\exp(\theta_i/T) - 1}, \qquad (7)$$

where θ_i and X_i are constants, given by $\theta_1 = 200$ K, $\theta_2 = 880$ K, $\theta_3 = 2137.5$ K, $X_1 = 0.4369 \times 10^{-7}$ K^{-1}, $X_2 = 15.7867 \times 10^{-7}$ K^{-1}, $X_3 = 42.5598 \times 10^{-7}$ K^{-1}. The linear thermal expansion coefficient is defined as $\alpha_T = \partial \varepsilon_T / \partial T$. α_T is about 10^{-6} K^{-1} at $T = 300$ K, but rises to $\sim 2 \times 10^{-6}$ K^{-1} at $T = 500$ K, and to $\sim 4 \times 10^{-6}$ K^{-1} at $T = 900$ K, and keeps on rising with higher temperature, according to equation (7). For high-temperature calculation, equation (7) is necessary. The thermal strain and linear thermal expansion coefficient are plotted against temperature in Fig. 2.

The thermal energy density U_T is obtained by numerically integrating $\int \rho C_v \, dT$ with tabulated values of specific heat C_v up to $T = 3000$ K (Reeber & Wang, 1996). C_v is small at low temperatures. It rises rapidly at around room temperature up to about 1000 K, but saturates then at elevated temperatures. For $T > 3000$ K, C_v is set to be constant, equal to the value at $T = 3000$ K. The thermal conductivity $\kappa = 2200$ W m^{-1} K^{-1} for diamond at 300 K. However, it decreases rapidly with increasing temperature. It drops to only about 100 W m^{-1} K^{-1} at $T = 2000$ K. The data of Wei et al. (1993) from 300 K to 2000 K are averaged and fit to a power law: $\kappa = 23.9 \times 10^6 \, T^{-1.63}$ for simplicity. It is used in the following simulations. The specific heat and heat conductivity are plotted against temperature in Fig. 3.

Other materials constants are given as density $\rho = 3.51$ g cm^{-3}, shear modulus $G = 508$ GPa and bulk modulus $K_b = 678$ GPa. For the range of thermal and mechanical loading under consideration, the density and moduli may be reasonably assumed to be constant. These values of G and K_b
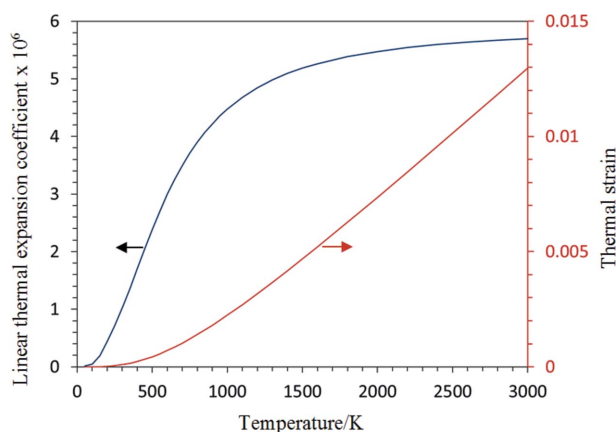
Figure 2
Variation of thermal strain (right) and linear thermal expansion coefficient (left) with temperature.

Figure 3
Variation of thermal conductivity and specific heat with temperature.

correspond to Young's modulus equal to 1220 GPa and the Poisson ratio equal to 0.2 (Spear & Dismukes, 1994, p. 4). The radiation heat transfer in the crystal layer and the radiation heat loss at the side surfaces are neglected; if considered, they would effectively shorten somewhat the thermal relaxation time.

The corresponding dilatational, shear and surface (Rayleigh) wave speeds are equal to 18.6, 12.0 and 10.9 km s^{-1}, respectively. The thermal diffusivity is equal to 12.2 cm^2 s^{-1} at $T = 300$ K, 1.5 cm^2 s^{-1} at $T = 600$ K, 0.5 cm^2 s^{-1} at $T = 1000$ K and 0.14 cm^2 s^{-1} at $T = 2000$ K, based on the above values of κ and C_v. These values are useful for estimating the characteristic time/length scales of various events of stress wave emission and propagation and thermal relaxation.

3. Simulation results and discussion

3.1. Transient thermal transfer analyses

3.1.1. Single-pulse input. We first describe the results of transient thermal transfer from the simulation of a single-pulse input with pulse energy $I_0 = 100$ µJ. The Gaussian beam size is set to be $a = 20$ µm. The attenuation length $L = 50$ µm, corresponding to an X-ray energy of $\sim$3.5 keV. The crystal plate thickness $h = 40$ µm, which is at the lower end for the diamond crystals used for X-ray FEL self-seeding due to large absorption for such low-energy photons ($\sim$4 keV). In this case, the laser energy absorbed by the crystal is about 55%. As the laser energy decreases, it raises the internal energy at the front surface by about 2.2 times that at the back surface. This energy deposition field is added to the initial field, and the simulation begins. Twenty equal divisions are used to discretize the domain in the thickness direction. An adaptive mesh is used in the radial direction, with ten equal divisions in the near 10 µm distance, and 200 unequal divisions of increasing size outwards by gradient 1.015 in the following 1490 µm distance, from the center. The time step is 1 ns. We carried out the purely thermal transfer analysis by solving equation (3) after idling the mechanical terms. This allows us to simulate the
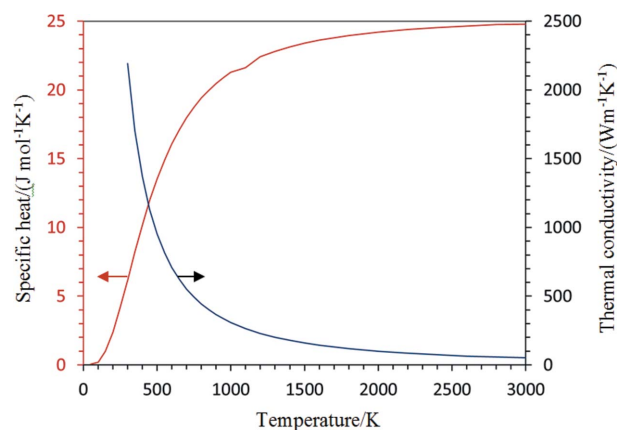
process in a much longer timescale than the later transient thermal stress wave case. It is justified that the stress field should have a trivial effect on the thermal conduction process, which involves a different amount of energy by orders of magnitude.

Selected results are presented in Figs. 4 and 5. Figs. 4(a)–4(f) show snapshots of the thermal field at various times in 100 ns increments. Fig. 5 shows the time evolution of the temperature (minus the initial temperature of 300 K) at three different radial distances, $r = 0$, 20 and 50 µm, on the front and back surfaces, $z = 0$, and 40 µm up to 100 µs. For a diffusion coefficient equal to $\sim$10 cm^2 s^{-1}, the time of 100 µs corresponds to a diffusion distance of a small fraction of a millimeter. Thus, the simulation domain is wide enough to avoid any remote boundary effects.

It can be seen in Fig. 4 that the early temperature is higher on the front surface than on the back surface due to laser attenuation. However, the temperature difference is smaller than 2.2 times the internal energy mentioned earlier. This is because the specific heat capacity of diamond varies sensitively with temperature below 1000 K (Reeber & Wang, 1996), as shown in Fig. 3. The initial highest temperature is 2315 K at the center on the front surface. It drops nearly linearly in the early 150 ns, and slightly more rapidly in the following 300 ns, and then the thermal relaxation rate decreases gradually. The thermal relaxation is undertaken over about 1000 ns across the thickness, as indicated by the convergence of the temperature histories on the front and back surfaces in Fig. 5. In the radial direction, it occurs on a similar time scale over the laser heating spot, as also shown in Fig. 5, but extends to a much longer time scale over a plate size of millimeters. However, since the laser energy is small when averaged over the entire effective volume, the temperature rise is only $\sim$1.5 K after 30 µs and $\sim$0.4 K after 100 µs near the laser impinging spot. It would continue to decrease over a longer period. It might be worth noting that we carried out the same simulation but with a constant thermal conductivity equal to the room-temperature value for all temperatures and compared the results. It was found that the true thermal relaxation presented herein is much slower, especially inside
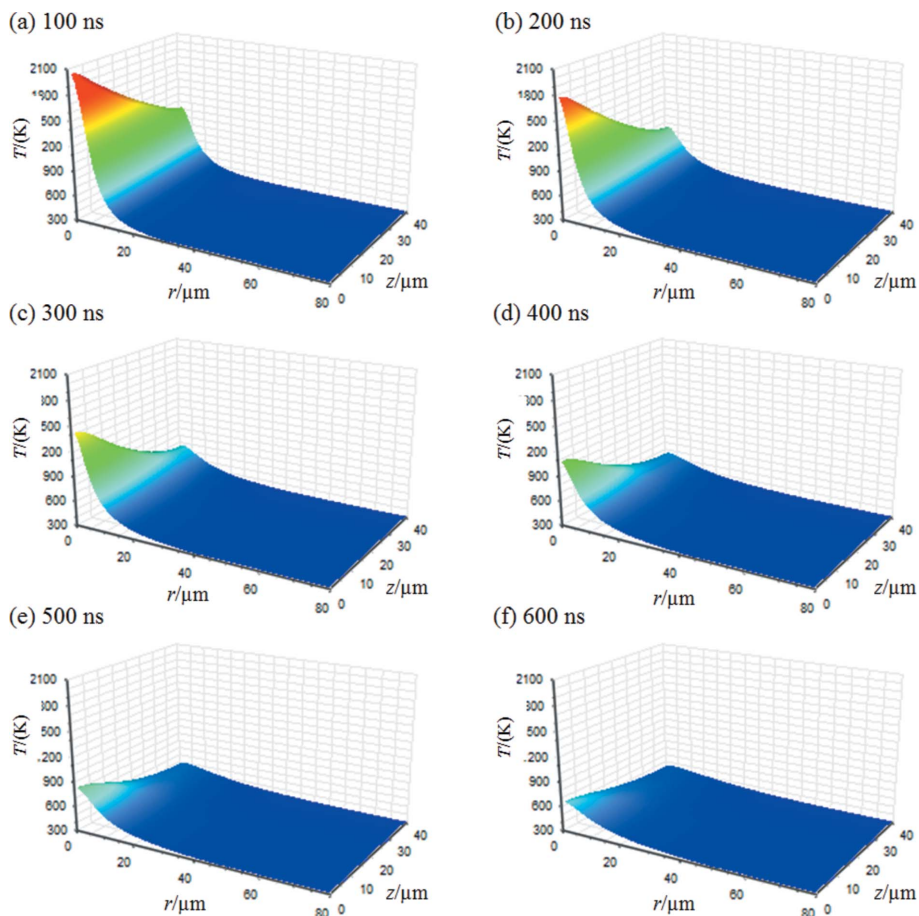
Figure 4
Snapshots of the temperature field in a 40 μm-thick diamond plate upon a single-pulse laser of 20 μm waist-size at various times in 100 ns increments.

the laser spot at elevated temperatures at the short timescale. For instance, the relaxation time of an uneven thermal field in the through-thickness direction is different by one order of magnitude, reflecting the strong temperature dependence of the thermal diffusivity. Thus, if the realistic material constants
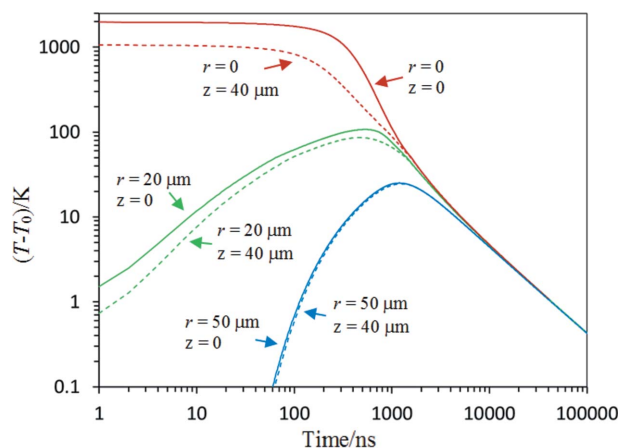

Figure 5
Time histories of temperature at three different distance $r = 0, 20, 50$ μm on the front surface ($z = 0$, solid) and back surface ($z = 40$ μm, dashed) in a 40 μm-thick diamond plate upon a single-pulse laser of 20 μm waist-size.

are not considered, it would substantially underestimate the adverse effects of the heat load of the laser pulses.

3.1.2. Multiple-pulse input. Motivated by the current pursuit of FELs at high repetition rates (Raubenheimer, 2014; Tsentscher *et al.*, 2006), we ran simulations of transient heat transfer at four different repetition rates, 0.1, 0.2, 0.5 and 1 MHz. All the parameters are the same as those in the above case, but the energy of individual laser pulses is added to the system periodically according to the repetition rates. The simulations are run over a period of 200 μs, respectively 20, 40, 100 and 200 pulses in total in the four cases. The time histories of the temperature at radial distances $r = 0$, 20 and 50 μm on the front surface $z = 0$ are recorded and plotted in Figs. 6(a)–6(d). Although the mechanical deformation and stress wave effects are excluded, it can be expected that similar wave dynamics are being generated by each pulse. On the other hand, the stress waves should have a trivial effect on the heat transfer due to the great difference of thermal energy *versus* mechanical energy, even though the deformation energy is seen to be partially converted back to thermal energy, as discussed later.

As shown in Figs. 6(a)–6(d), the temperature within the laser spot rises instantaneously upon each shot. It evolves over time in a similar way to the above single-shot case. However, each shot would have some residual thermal energy left behind, and the temperature that each shot sees keeps on rising, due to the finite thermal conductivity. This effect raises the practical question at what repetition rate the residual heat effect would become non-trivial to affect the optical performance of the crystal plate. The answer should depend on how the optical component operates in a specific case and it is not our intent here to provide it. In the four cases analyzed, the residual temperatures that the second pulse sees are 304.7 K, 310.3 K, 334.4 K and 411.1 K, respectively, worsening rapidly when the repetition rate reaches near the MHz level. In particular, a runaway temperature increase is observed after only a few pulses in the case of 1 MHz. For the case of 500 kHz, the temperature seems to have ratcheted up ready for a runaway rise after 100 pulses. For the other two cases of 100 and 200 kHz, the residual temperature that each pulse sees increases more slowly. The runaway temperature rise upon a threshold temperature level is explained by the fact that the thermal conductivity (more precisely, the thermal diffusivity) of diamond decreases rapidly with increasing temperature [by a power law which we use to roughly fit the experimental data

(Reeber & Wang, 1996)]. When the temperature becomes sufficiently high, the dissipation rate is lowered so much, while the energy input rate is maintained constant, as to result in a thermal blowout, *i.e.* a spontaneous hotspot. This rapid temperature increase may lead to local permanent damage to the diamond if no other dissipation mechanism is instated. In the two cases of 100 and 200 kHz, a steady state of competing heat deposition and heat damping may not be reached before the runaway instability occurs and hence before the material is damaged, unlike the typical expectation of a steady state in previous gas attenuator simulations (Feng *et al.*, 2016; Yang *et al.*, 2017). Again, we ran the same simulations but with constant thermal conductivity set to be the room temperature value for comparison. It was found that the temperature rise scales linearly with the number of pulses, N, in the early few to tens of pulses, but scales as $\log(N)$ afterwards. It is very different from the runaway phenomenon described above when the more realistic material constants are considered, again suggesting the necessity to use realistic material properties for meaningful analysis.

Figure 6
Time histories of temperature at three different distance $r = 0$ (red), 20 (green), 50 µm (blue) on the front surface ($z = 0$) in a 40 µm-thick diamond plate under continuous pulses at various repetition rates: (*a*) 100 kHz; (*b*) 200 kHz; (*c*) 500 kHz; (*d*) 1 MHz.

3.2. Transient thermal stress wave analyses

We ran simulations for transient thermal stress wave analysis for four cases with different diamond thickness h or laser spot size a: $h = 10$ µm, $a = 20$ µm; $h = 20$ µm, $a = 20$ µm; $h = 40$ µm, $a = 20$ µm; $h = 10$ µm, $a = 100$ µm. Only a single pulse input is examined, with common pulse energy $I_0 = 100$ µJ and attenuation length $L = 50$ µm, the same as above. For $h = 10$ µm, 20 µm and 40 µm, the laser energy is about 18%, 32% and 55%, respectively, absorbed by the crystal. Twenty, 30 and 40 equal divisions, respectively, are used to discretize the domain in the thickness direction for these three thicknesses. An adaptive mesh is used in the radial direction. Twenty equal divisions are used in the near 10 µm distance, and 600 unequal divisions with increasing size by gradient 1.003 in the following 790 µm distance, for a laser spot size of 10 µm. One hundred equal divisions are used in the near 50 µm distance, and 650 unequal divisions with increasing size by gradient 1.003 in the following 850 µm distance, for a laser spot size of 50 µm. The time step is 10 ps for all of the cases. It was checked that this time step is fine enough to generate reasonably accurate results compared with time steps of 2.5 and 5 ps. The stress waves would propagate by <0.2 µm in space each time step, smaller than the spatial grid size. Since we use an implicit finite-difference scheme for time integration and an iterative algorithm for coping with non-linear effects in thermal energy,
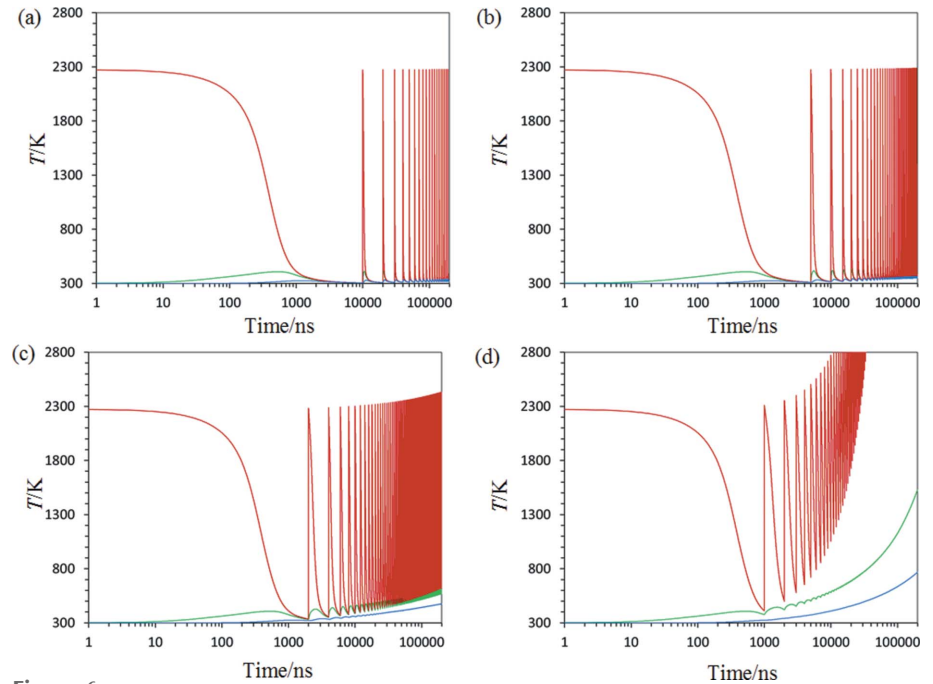
thermal strain and heat conduction, which are all coupled, the solution is unconditionally stable. The simulation is terminated at $t = 40$ ns before the emitted stress waves reach the simulation domain boundary. Selected results are plotted in Figs. 7, 8 and 9.

The total deformation energy, $\int_V U_\varepsilon \, \mathrm{d}V$, the total kinetic energy $\int_V (1/2)\rho\mathbf{v} \cdot \mathbf{v} \, \mathrm{d}V$, and the change of thermal energy, $\int_V (U_\mathrm{T} - U_\mathrm{T0}) \, \mathrm{d}V$, are calculated at each time step, where V is the domain and U_T0 is the initial thermal energy density upon the laser energy deposition. The r-component and z-component of kinetic energy, $\int_V (1/2)\rho v_r^2 \, \mathrm{d}V$ and $\int_V (1/2)\rho v_z^2 \, \mathrm{d}V$, are also calculated, representing the wave activity in the two corresponding directions, respectively. They are shown in Figs. 7(*a*)–7(*d*), respectively, for the four cases. Some snapshots of the velocity fields at $t = 0.1, 0.5, 1, 2$ and 3 ns are captured and plotted in Figs. 8(*A*)–8(*E*) and Figs. 8(*a*)–8(*e*) for the case of $h = 40$ µm, $a = 20$ µm. In the left-hand column, (*A*)–(*E*), the three-dimensional (3D) surface plot is used to show the velocity component v_z, and the color code to indicate strain component ε_{zz}. In the right-hand column, (*a*)–(*e*), the 3D surface plot is used to show the velocity component v_r, and the color code to indicate strain component ε_{rr}. Similarly, snapshots at $t = 0.1, 0.3, 0.5, 1.5$ and 3 ns are captured and plotted in Figs. 9(*A*)–9(*E*) and Figs. 9(*a*)–9(*e*) for the case of $h = 10$ µm, $a = 20$ µm. The other two cases are also examined but not shown here.

3.2.1. Case study with $h = 40$ µm, $a = 20$ µm. In this case, 55% of the laser energy, *i.e.* 55 µJ out of 100 µJ, is deposited into the diamond. Amongst this, the majority is stored in the form of thermal energy, but only 0.36 µJ is stored in the form of deformation energy due to thermal strain, as shown at $t = 0$
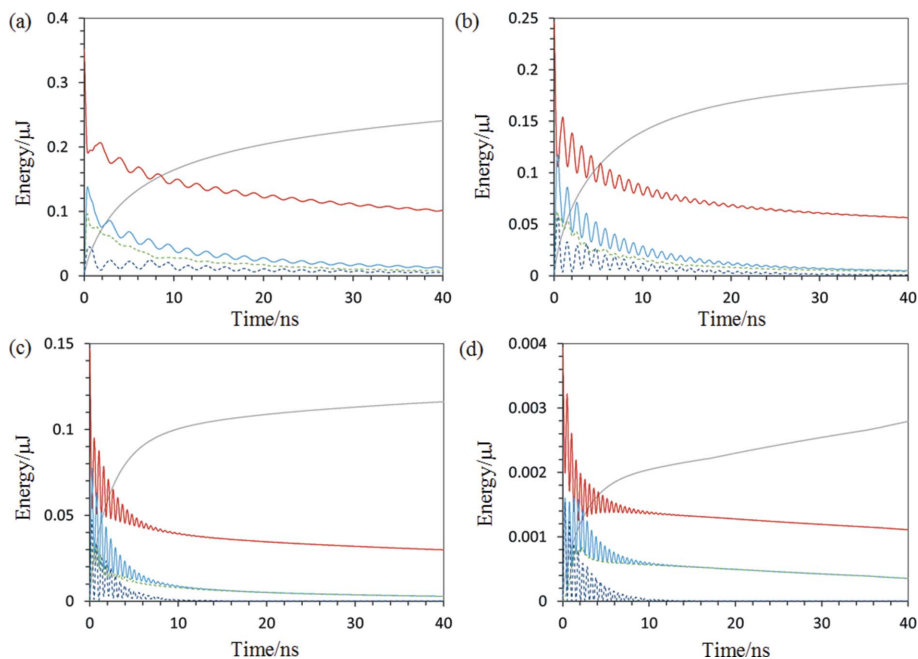
Figure 7
Time histories of thermal energy change (gray solid), deformation energy (red solid) and total (blue solid), r-portion (green dashed) and z-portion (purple dashed) of kinetic energy in a diamond plate upon a single-pulse laser of thickness h and waist-size a: (a) h = 40 μm, a = 20 μm; (b) h = 20 μm, a = 20 μm; (c) h = 10 μm, a = 20 μm; (d) h = 10 μm, a = 100 μm.

in Fig. 7(a). It is this seemingly tiny deformation energy that launches stress waves with particle velocities reaching over 200 m s^{-1}. The stress wave emission is different in the through-thickness z-direction and in the radial r-direction. In the z-direction, the stress waves, which are dilatational, break out at the two traction-free side surfaces and propagate inwards, as seen in the left-hand column of Fig. 8. In the r-direction, it is more complicated because the radial strain gradient drives dilatational wave emission in the middle portion propagating at the longitudinal wave speed equal to 18.6 km s^{-1}. Near the surfaces, Rayleigh surface waves are emitted propagating at a Rayleigh wave speed equal to 10.9 km s^{-1}, which is much slower, resulting in a complicated wave pattern, as seen in the right-hand column of Fig. 8.

Subsequently the radial dilatational and surface waves propagate cylindrically outwards. In contrast, the early dilatational waves in the z-direction are quickly shattered by radial shear wave emission due to the surrounding constraint. This effect is significant due to the large plate thickness compared with the laser transverse radius, with ratio 4:1. Only the deformation energy in a shallow depth can be released in this mode. It quickly results in a rugged v_z field. While this mode of thermal strain relaxation is ineffective, it takes a long time for the stress waves in the z-direction to die out relative to other cases in Figs. 7(c) and 7(d), which will be discussed more in the following.

During the stress wave emission, the initial thermal strain energy is partially converted into kinetic energy. As can be seen in Fig. 7(a), the kinetic energy peaks at 70 nJ at t = 0.6 ns, but then gradually decreases. The peak time corresponds to a wave travel distance of ~10 μm, consistent with the laser

transverse radius. It is thus the stress wave emission time, as expected. At the same time, the deformation energy also decreases, but the thermal energy increases. The deformation energy and kinetic energy (as well as the thermal energy) oscillate out of phase indicating their constant exchange back and forth due to the wave reflection at the side surfaces. Surprisingly, at this short time scale, the thermal field evolves fast enough to affect the mechanical wave event; that is, as the temperature field evolves, the thermal strain field relaxes, resulting in conversion/dissipation of mechanical energy into thermal energy and entropy increase. Since no other dissipative mechanism (such as viscosity) is introduced, the mechanical energy would no longer decay after the stress waves propagate out of the hot zone. This is important because it means that each laser pulse would generate a certain amount of 'permanent' kinetic energy in the crystal plate. Its potential consequence to vibration under multiple laser pulses will be discussed later. At t = 40 ns, there remains about 12 nJ kinetic energy in the system; it is still dropping slightly but is expected to reach a steady value soon.

3.2.2. Aspect ratio effects. By comparing Figs. 7(a)–7(c), and Figs. 8 and 9, it can be seen that the stress wave emission process is different in the cases of different thicknesses but same laser spot size. In the thick-layer case, the laser-heated volume is pencil-like, in which the through-thickness dilatational stress waves only manifest themselves near the surfaces in a shallow volume and are rapidly shattered due to the surrounding constraint. There is not much oscillation seen in the evolution of the energy terms in Fig. 7(a). In contrast, in the thin-layer cases, the heated volume is more like a thin disc. The through-thickness dilatational stress waves can be emitted more freely and sustained as a planar wave within the heated zone (Stoupin et al., 2012). The mechanical energy stored in the through-thickness dilatational stress waves are drained by emitting shear and dilatational stress waves outwards in the radial direction at the boundary of the heated zone. Due to the longer perimeter of the hot–cold front, this energy conversion process is more efficient in the thin-layer case. The z-component of the kinetic energy diminishes at t = 10 ns as shown in Fig. 7(c). In contrast, it remains non-trivial (relative to the amplitude at the beginning) at the same time in the thick-layer cases as shown in Figs. 7(a) and 7(b), although it dies out soon after.

When the same amount of heat is deposited over a wider laser spot, the initial temperature is substantially reduced. The initial thermal deformation energy is even more substantially reduced because of the much lower thermal expansion coefficient at lower temperature. It reduces by three orders of

magnitude when the laser spot size increases by five times, as seen in Figs. 7(a) and 7(d). Despite the much reduced intensity, the stress wave emission remains unchanged characteristically except for the time of the kinetic energy to reach its

peak. In the cases of $a = 20$ μm [Figs. 7(a)–7(c)], the kinetic energy peaks at the first wave oscillation, even for the thinnest case [Fig. 7(c)]. In contrast, it peaks after four wave oscillations in the case of $a = 100$ μm [Fig. 7(d)], indicating the different time scales of stress wave emission along the through-thickness direction from that along the z-direction.

After the stress waves are moved out of the hot zone, they survive for a long time due to the lack of an intrinsic dissipation mechanism such as viscosity in diamond. Most importantly, this study demonstrates that a certain amount of kinetic energy can be left 'permanent' in the system by each laser pulse. From Figs. 7(a)–7(d), the amount of kinetic energy can be seen to strongly depend on the laser spot size and the deposited energy (i.e. thickness). The next question is whether vibrations and similar would cause problems if the plate is not properly mounted.

3.3. Vibrational analysis

Based on the above transient dynamic analysis, it is clear that the instantaneous laser energy deposition would locally raise the temperature during its passage and introduce thermal strain. The linear thermal expansion coefficient in diamond is small at low temperature but can increase dramatically at high temperature upon absorption of soft X-rays. The thermal strain can generate stress waves. After the stress waves propagate out of the hot zone, the kinetic energy carried by them becomes 'permanent' in the diamond due to a lack of other intrinsic dissipation mechanisms such as viscosity. If no appropriate passive damping is instated, the kinetic energy would cumulate pulse after pulse. For the sake of an estimate by order of magnitude, the kinetic energy may be reasonably set to be 10 nJ for a laser spot size of 20 μm and a fraction of nJ for a laser spot size of 100 μm, from a deposited energy of tens of μJ per pulse, as indicated in the examples analyzed above. The question is at what amplitude it may drive a diamond plate to vibrate at a given frequency.

We conducted a modal analysis of a thin diamond layer, 3 mm × 5 mm, in-

Figure 8
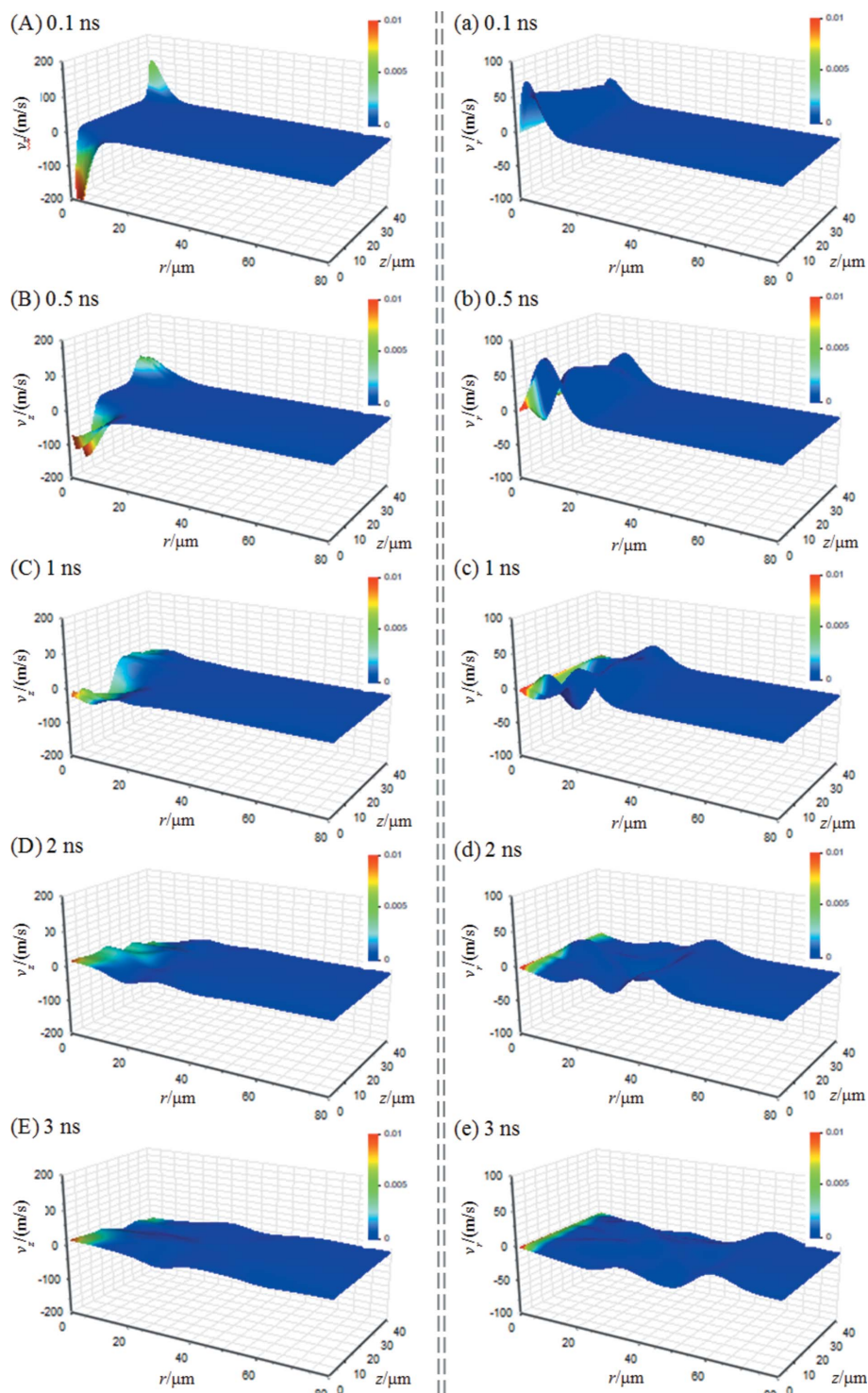Snapshots of stress waves emission in a 40 μm-thick diamond plate upon a single-pulse laser of 20 μm waist-size at various times: (A,a) 0.1 ns; (B,b) 0.5 ns; (C,c) 1 ns; (D,d) 2 ns; (E,e) 3 ns. In the left-hand column (A)–(E), the 3D profiles show the field of velocity component v_z, and the color code indicates the field of strain component ε_{zz}. In the right-hand column (a)–(e), the 3D profiles show the field of velocity component v_r, and the color code indicates the field of strain component ε_{rr}.
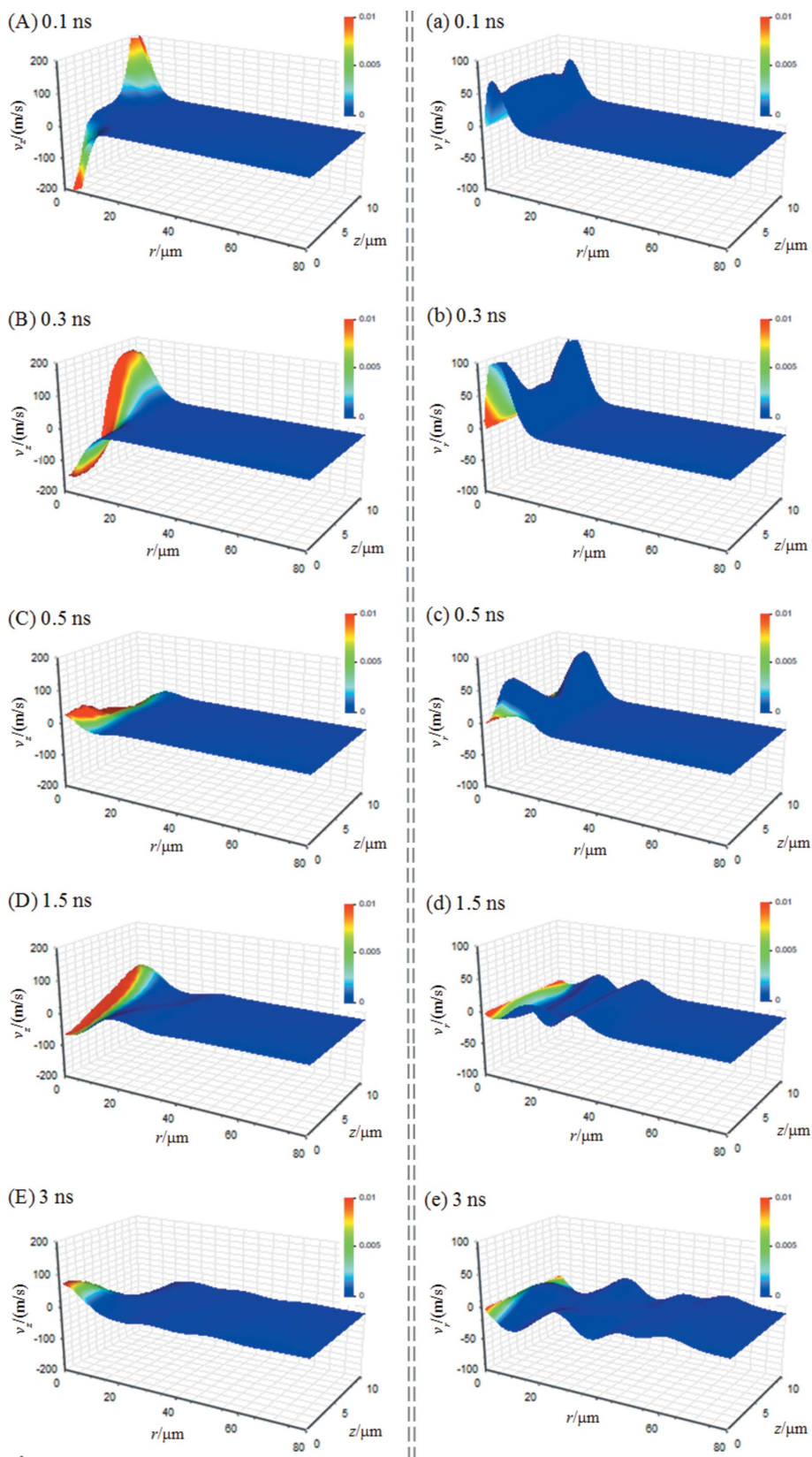
Figure 9
Snapshots of stress waves emission in a 10 μm-thick diamond plate upon a single-pulse laser of 20 μm waist-size at various times: (A,a) 0.1 ns; (B,b) 0.3 ns; (C,c) 0.5 ns; (D,d) 1.5 ns; (E,e) 3 ns. In the left-hand column (A)–(E), the 3D profiles show the field of velocity component v_z, and the color code indicates the field of strain component ε_{zz}. In the right-hand column (a)–(e), the 3D profiles show the field of velocity component v_r, and the color code indicates the field of strain component ε_{rr}.

plane and of various thicknesses, using the finite-element software package *ANSYS*. Free vibrations and vibrations with one edge fixed were analyzed. The natural frequencies were acquired up to 5 MHz. The number of vibrational states for the 40 μm-thick case is plotted in Fig. 10. The insets are the first and second mode shapes, as directed by the arrows pointing to the corresponding frequencies. The first mode frequencies are plotted as a function of thickness in Fig. 11. The first mode frequencies depend linearly on the thickness. For the thinnest plate, 10 μm-thick, the first mode frequency is 1500 Hz in the fixed case and 6940 Hz in the free case. These frequencies are one order of magnitude higher than the repetition rate of 120 Hz at the Linac Coherent Light Source (LCLS) (Amann *et al.*, 2012). However, it should be noted that, if the plate is not properly constrained, the null modes of rigid body motion can be active. For instance, if a plate is placed against a wall or a trench it would move like a pendulum. In this case, the frequency may be estimated by $(g/L)^{1/2}$, where L is the characteristic length (plate size) and g is the acceleration due to gravity; setting $L = 1$ mm, the frequency is ∼100 Hz, near the LCLS repetition rate.

The energy of a plate vibrating at angular frequency ω may be expressed by $(1/2)M\omega^2\bar{u}^2$, where M is the total mass and $\bar{u}$ can be understood as a measure of the vibration amplitude. For a diamond plate of dimensions 5 mm × 3 mm × 0.04 mm, the mass $M = 2.11$ mg. From the above dynamic simulation, each pulse of 100 μJ with one half deposited would generate, for example, 10 nJ of kinetic energy. For only one shot, the plate would vibrate by about 1 mm in amplitude for a frequency of 100 Hz, scaled by $1/\omega$. For frequencies up to 1 MHz, the vibrational amplitude would drop below 1 μm for a single shot. However, the vibration may be excited and reach harmful levels over tens to hundreds of shots. It might be worth noting again that the vibrational states are populated linearly with frequency after thousands to tens of thousands Hertz depending on the plate thickness, as shown in Figs. 10 and 11.
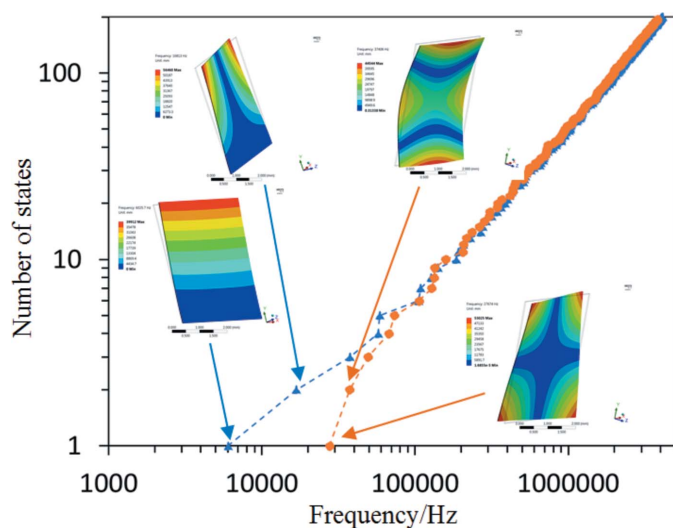
Figure 10
Number of vibrational states as a function of frequency for a free plate (circles) and a plate fixed at one edge (triangles). The insets illustrate the mode shapes at the first and second modes of each case, as directed by the arrows to the frequencies.
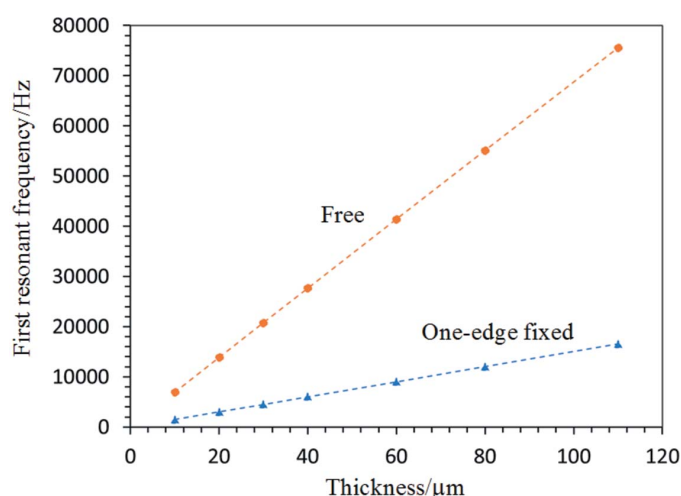

Figure 11
First natural frequency as a function of thickness for a free plate and plate with one edge fixed.

Any operational frequency above this threshold would be surrounded by many resonant modes, resulting in vibrational excitation. If a motion steadiness at a vibration level better than tens of micrometers is required, passive damping or other intrinsic damping mechanisms must be introduced to mitigate the effect.

4. Conclusions

We have performed a computational study of the transient thermal stress wave emission and thermal conduction in a thin diamond crystal under high-intensity laser shock. The resonant vibration has also been examined. The problem is formulated on the continuum mechanics. The transient dynamic analysis is based on an in-house code. The modal analysis is conducted by using the commercial finite-element software package *ANSYS*. Cases of various laser spot size and plate thickness are analyzed. This reveals the transient dynamics of both mechanical deformation and thermal transfer and the energy transfer mechanisms among the thermal energy, strain energy and kinetic energy. It is shown that the radial dilatational stress wave emission dominates, which is driven by the radial thermal gradient. The main stress wave emission is completed in a fraction of a nanosecond or several nanoseconds for laser spot sizes of 20 μm or 100 μm, respectively. It then takes tens of nanoseconds for the through-thickness dilatational stress waves to diminish by emitting radial dilatational and shear stress waves due to the coupling of the different mechanical deformation components. In the case of a thick layer relative to the laser spot size, the heated volume is pencil-like, and the through-thickness dilatational stress waves are confined to the surface. In contrast, they are generated more freely within the heated zone in the thin layer case where the heated volume is more like a thin disc. Consequently, the relaxation of wave activity is more efficient in the thin layer case of an effectively longer perimeter along the hot–cold front. The stress waves are conserved in energy after propagating out of the hot zone due to the lack of an intrinsic dissipative mechanism such as viscosity in diamond. This results in the emission of a certain amount of 'permanent' kinetic energy in the system. It is also found that the thermal relaxation effect is already apparent during the time scale of stress wave events. This leads to a continuous conversion of the mechanical energy back to thermal energy. The transient thermal conduction has also been analyzed under multiple pulses at various repetition rates. It is shown that the temperature that the next pulse sees increases rapidly with the number of pulses, especially when the repetition rate is near the MHz range, for a typical laser pulse energy of the LCLS. Finally, it was shown that the resonant frequencies start at the thousands of Hz to tens of thousand of Hz range depending on thickness. They are populated linearly in terms of frequency. The potential vibrational amplitude is estimated as a function of frequency, given an amount of kinetic energy. It was shown that, for the amount of kinetic energy predicted above from the transient dynamic analysis, the vibrational amplitude can be harmful at the LCLS at a repetition rate of 120 Hz if the plate is not properly constrained. For high repetition rates, the vibrational amplitude is trivial in the case of a single shot, but can add up to a harmful level too after tens to hundreds of pulses. These results should be helpful in the design of monochromators and spectrometers based on thin diamond crystals for high-intensity XFEL applications at high repetition rates.

References

Amann, J., Berg, W., Blank, V., Decker, F.-J., Ding, Y., Emma, P., Feng, Y., Frisch, J., Fritz, D., Hastings, J., Huang, Z., Krzywinski, J., Lindberg, R., Loos, H., Lutman, A., Nuhn, H.-D., Ratner, D., Rzepiela, J., Shu, D., Shvyd'ko, Y., Spampinati, S., Stoupin, S., Terentyev, S., Trakhtenberg, E., Walz, D., Welch, J., Wu, J., Zholents, A. & Zhu, D. (2012). *Nat. Photon.* **6**, 693–698.

Donaldson, B. K. (2006). *Introduction to Structural Dynamics.* Cambridge University Press.

Emma, P., Akre, R., Arthur, J., Bionta, R., Bostedt, C., Bozek, J., Brachmann, A., Bucksbaum, P., Coffee, R., Decker, F.-J., Ding, Y., Dowell, D., Edstrom, S., Fisher, A., Frisch, J., Gilevich, S., Hastings, J., Hays, G., Hering, P., Huang, Z., Iverson, R., Loos, H., Messerschmidt, M., Miahnahri, A., Moeller, S., Nuhn, H.-D., Pile, G., Ratner, D., Rzepiela, J., Schultz, D., Smith, T., Stefan, P., Tompkins, H., Turner, J., Welch, J., White, W., Wu, J., Yocky, G. & Galayda, J. (2010). *Nat. Photon.* **4**, 641–647.

Feng, Y., Krzywinski, J., Schafer, D. W., Ortiz, E., Rowen, M. & Raubenheimer, T. O. (2016). *J. Synchrotron Rad.* **23**, 21–28.

Geloni, G., Kocharyan, V. & Saldin, E. (2011). *J. Mod. Opt.* **58**, 1391–1403.

Ishikawa, T., Aoyagi, H., Asaka, T., Asano, Y., Azumi, N., Bizen, T., Ego, H., Fukami, K., Fukui, T., Furukawa, Y., Goto, S., Hanaki, H., Hara, T., Hasegawa, T., Hatsui, T., Higashiya, A., Hirono, T., Hosoda, N., Ishii, M., Inagaki, T., Inubushi, Y., Itoga, T., Joti, Y., Kago, M., Kameshima, T., Kimura, H., Kirihara, Y., Kiyomichi, A., Kobayashi, T., Kondo, C., Kudo, T., Maesaka, H., Maréchal, X. M., Masuda, T., Matsubara, S., Matsumoto, T., Matsushita, T., Matsui, S., Nagasono, M., Nariyama, N., Ohashi, H., Ohata, T., Ohshima, T., Ono, S., Otake, Y., Saji, C., Sakurai, T., Sato, T., Sawada, K., Seike, T., Shirasawa, K., Sugimoto, T., Suzuki, S., Takahashi, S., Takebe, H., Takeshita, K., Tamasaku, K., Tanaka, H., Tanaka, R., Tanaka, T., Togashi, T., Togawa, K., Tokuhisa, A., Tomizawa, H., Tono, K., Wu, S., Yabashi, M., Yamaga, M., Yamashita, A., Yanagida, K., Zhang, C., Shintake, T., Kitamura, H. & Kumagai, N. (2012). *Nat. Photon.* **6**, 540–544.

LeVeque, R. J. (2002). *Finite Volume Methods for Hyperbolic Problems*, Vol. 31. Cambridge University Press.

Mura, T. (1987). *Micromechanics of Defects in Solids.* Dordrecht: Martinus Nijhoff.

Navirian, H. A., Schick, D., Gaal, P., Leitenberger, W., Shayduk, R. & Bargheer, M. (2014). *Appl. Phys. Lett.* **104**, 021906.

Raubenheimer, T. (2014). *Proceedings of the 36th International Free-Electron Laser Conference (FEL2014)*, 25–29 August 2014, Basel, Switzerland.

Reeber, R. R. & Wang, K. (1996). *J. Electron. Mater.* **25**, 63–67.

Rehanek, J., Makita, M., Wiegand, P., Heimgartner, P., Pradervand, C., Seniutinas, G., Flechsig, U., Thominet, V., Schneider, C. W., Fernandez, A. R., David, C., Patthey, L. & Juranić, P. (2017). *J. Instrum.* **12**, A07001.

Shorr, B. F. (2015). *Thermal Integrity in Mechanics and Engineering.* Berlin: Springer.

Shvyd'ko, Y., Blank, V. & Terentyev, S. (2017). *MRS Bull.* **42**, 437–444.

Spear, K. E. & Dismukes, J. P. (1994). *Synthetic Diamond: Emerging CVD Science and Technology*, Vol. 25. John Wiley and Sons.

Stoupin, S., March, A. M., Wen, H., Walko, D. A., Li, Y., Dufresne, E. M., Stepanov, S. A., Kim, K.-J., Shvyd'ko, Y. V., Blank, V. D. & Terentyev, S. A. (2012). *Phys. Rev. B*, **86**, 054301.

Tschentscher, T., *et al.* (2006). *Synchrotron Radiat. News*, **19**, 13–19.

Versteeg, H. K. & Malalasekera, W. (2007). *An Introduction to Computational Fluid Dynamics: the Finite Volume Method.* Pearson Education.

Wei, L., Kuo, P., Thomas, R., Anthony, T. & Banholzer, W. (1993). *Phys. Rev. Lett.* **70**, 3764–3767.

Yabashi, M., Hastings, J. B., Zolotorev, M. S., Mimura, H., Yumoto, H., Matsuyama, S., Yamauchi, K. & Ishikawa, T. (2006). *Phys. Rev. Lett.* **97**, 084802.

Yang, B., Wu, J., Raubenheimer, T. O. & Feng, Y. (2017). *J. Synchrotron Rad.* **24**, 547–559.

Zhu, D., Cammarata, M., Feldkamp, J. M., Fritz, D. M., Hastings, J. B., Lee, S., Lemke, H. T., Robert, A., Turner, J. L. & Feng, Y. (2012). *Appl. Phys. Lett.* **101**, 034103.

Zhu, D., Feng, Y., Stoupin, S., Terentyev, S. A., Lemke, H. T., Fritz, D. M., Chollet, M., Glownia, J. M., Alonso-Mori, R., Sikorski, M., Song, S., van Driel, T. B., Williams, G. J., Messerschmidt, M., Boutet, S., Blank, V. D., Shvyd'ko, Y. V. & Robert, A. (2014). *Rev. Sci. Instrum.* **85**, 063106.